ACS APPLIED MATERIALS & INTERFACES
Research Article
www.acsami.org

Facet Cutting and Hydrogenation of In_2O_3 Nanowires for Enhanced Photoelectrochemical Water Splitting

Ming Meng,[†] Xinglong Wu,*[,†,§] Xiaobin Zhu,[†] Xiaoshu Zhu,[‡] and Paul K. Chu*[,§]

[†]National Laboratory of Solid State Microstructures and Department of Physics, Nanjing University, Nanjing 210093, P. R. China
[‡]Center for Analysis and Testing, Nanjing Normal University, Nanjing, 210093, P. R. China
[§]Department of Physics and Materials Science, City University of Hong Kong, Tat Chee Avenue, Kowloon, Hong Kong, China

S *Supporting Information*

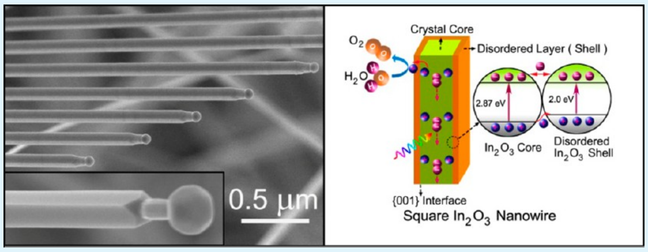

ABSTRACT: Semiconductor nanowires (NWs) are useful building blocks in optoelectronic, sensing, and energy devices and one-dimensional NWs have been used in photoelectrochemical (PEC) water splitting because of the enhanced light absorption and charge transport. It has been theoretically predicted that the {001} facets of body center cubic (bcc) In_2O_3 nanocrystals can effectively accumulate photogenerated holes under illumination, but it is unclear whether facet cutting of NWs can enhance the efficiency of PEC water splitting. In this work, the photocurrent of square In_2O_3 NWs with four {001} facets is observed to be an order of magnitude larger than that of cylindrical In_2O_3 NWs under the same conditions and subsequent hydrogen treatment further promotes the PEC water splitting performance of the NWs. The optimized hydrogenated In_2O_3 NWs yield a photocurrent density of 1.2 mA/cm^2 at 0.22 V versus Ag/AgCl with a Faradaic efficiency of about 84.4%. The enhanced PEC properties can be attributed to the reduced band gap due to merging of the disordered layer-induced band tail states with the valence band as well as improved separation of the photogenerated electrons/holes between the In_2O_3 crystal core and disordered layer interface. The results provide experimental evidence of the important role of facet cutting, which is promising in the design and fabrication of NW-based photoelectric devices.

KEYWORDS: *In_2O_3 nanowires, facet cutting, hydrogen treatment, water splitting*

■ INTRODUCTION

Photoelectrochemcial (PEC) water splitting utilizing semiconductor materials and solar energy is an environmentally friendly and economical energy conversion and storage process.[1,2] The photoanode, which is the heart of the system, plays a crucial role in the water splitting efficiency.[3] There has been extensive research on identifying new photoanode materials and structures to improve the efficiency, for instance, by doping wide band gap semiconductors such as TiO_2 and ZnO to obtain visible-light photocatalytic activity,[4−6] preparation of novel heterojunctions,[7−9] design of new structures and morphologies including one-dimensional (1D) nanostructures and 2D nanoflakes,[3,10−12] and addition of cocatalysts such as cobalt phosphate.[13] 1D semiconductor nanostructures such as nanowires (NWs),[14] nanotubes (NTs),[15] and nanorods (NRs)[3,16] have been employed in PEC water splitting because of the enhanced light absorption and charge transport.[17−20] Unfortunately, photogenerated electron−hole pairs tend to recombine on the surface of cylindrical NWs[21] because there is a lack of specific crystal facets to accumulate electrons or holes thus reducing electron−hole separation compared to polyhedral nanoparticles (NPs). It has been recently shown by the nanocrystal cutting theory[22] that the photocatalytic activity is closely related to the specific crystal facets on nanomaterials such as In_2O_3,[23] Cu_2O,[24,25] and TiO_2 polyhedrons.[26] Because photogenerated electrons and holes are expected to accumulate on different crystal facets as a result of the difference in the energy levels among different crystal faces,[27,28] it is believed that proper facet cutting of nanostructured photoanode materials will enhance the PEC performance.

Indium oxide (In_2O_3) possesses a favorable energy band structure with the conduction band (CB) bottom at −0.63 V versus the normal hydrogen electrode (NHE) of the hydrogen evolution potential and the valence band (VB) at +2.17 V versus NHE of the oxygen evolution potential.[29] Although photoelectrodes made of In_2O_3 thin films and particles have been reported, PEC water splitting on In_2O_3 NW photoanodes has not been investigated systematically. In this work, In_2O_3 NWs with two different morphologies, square and cylindrical, are prepared and the effects of facet cutting on the PEC activity of the materials are compared and demonstrated.

Received: December 7, 2013
Accepted: February 25, 2014
Published: February 25, 2014

dx.doi.org/10.1021/am4056358 | *ACS Appl. Mater. Interfaces* 2014, 6, 4081−4088

■ EXPERIMENTAL SECTION

Sample Preparation. Indium oxide (In_2O_3) NWs were synthesized by chemical vapor deposition (CVD) utilizing a carbothermal reduction method. A mixture containing In_2O_3 (0.2 g) and active carbon (0.3 g) was ground for 10 min, loaded onto an alumina boat, and inserted into a quartz tube at the front end of a furnace. An n-type (100) Si sample (1−10 Ω•cm resistivity, 0.5 mm thick, and 1 × 1 cm^2 in size) coated with a 10 nm thick gold layer was placed downstream in the quartz tube. The furnace was heated to 1100 °C in 20 min and kept at this temperature for 2.5 h under a mixture of Ar (98%) and O_2 (2%) at a flow rate of 100 sccm. If the pressure in the growth chamber was 1 Torr, cylindrical In_2O_3 NWs were produced but if the pressure was 1 atm, square In_2O_3 NWs were prepared instead. After the system was cooled to room temperature, a light gray layer was deposited on the silicon substrate. The thickness of the layer determined on the Zeta 20 (Zeta Instruments, United States) was 25.7 μm. The In_2O_3 NWs coated with disordered layers were fabricated by annealing in a hydrogen atmosphere at 400, 500, and 600 °C. Prior to electrochemical measurements, an Ohmic contact was fabricated on the backside of the Si wafer.[23] The front side with the In_2O_3 film was painted with insulating epoxy resin except the working electrode area of about 0.8 cm^2.

Characterization. X-ray powder diffractometry (XRD, Philips, Xpert), field-emission scanning electron microscopy (FE-SEM, Hitachi S4800), high-resolution transmission electron microscopy (HR-TEM, JEOL-2100), and X-ray photoelectron spectroscopy (XPS, PHI5000 VersaProbe) were performed. The diffuse reflectance spectra were acquired on a VARIAN Cary5000 spectrophotometer. The PEC measurements were performed in a 1 M NaOH (pH 13.6) electrolyte using three electrodes connected to a CHI 660D (CH Instrument) (Figure S1 in the Supporting Information), with the In_2O_3 NW photoanode being the working electrode, Pt mesh the counter electrode, and Ag/AgCl (1 mol/L NaOH-filled) the reference electrode. A 500 W Xe lamp with a power of 270 mW/cm^2 illuminated the In_2O_3 NW photoanode surface and a water filter was utilized between the lamp and electrochemical cell to eliminate solution heating from the infrared light.

Oxygen Measurement. The evolved O_2 was quantitatively detected by an Ocean Optics oxygen sensor system equipped with a FOXY probe inserted into the headspace of the anodic compartment (NeoFox phase Measurement System). The experiments were performed in a similar manner as the photocurrent measurements (see Figure S1 in the Supporting Information). The headspace of the anodic compartment was purged with high purity N_2 (99.9995%) for 1 h under vigorous stirring. The measured gas production from the In_2O_3 NWs remained at 0.22 V versus Ag/AgCl for 150 min and the evolved amount of O_2 was corrected by Henry's law.

■ RESULTS AND DISCUSSION

By modulating the synthesis conditions, circular and square facet cutting of the NWs can be accomplished in a controllable fashion, as confirmed by powder XRD revealing that the pure In_2O_3 phase exists in all the samples. The XRD pattern in Figure S2 in the Supporting Information shows that all the diffraction peaks match those of the body center cube (bcc) structure of In_2O_3 (JCPDS card No. 06−416). The sharp and intense peaks also suggest that the In_2O_3 NWs are crystalline. The FE-SEM image of the cylindrical In_2O_3 NWs is depicted in Figure S3 in the Supporting Information. The low- and high-magnification FE-SEM images disclose densely packed cylindrical In_2O_3 NWs tens of micrometers long with diameters ranging from 100 to 200 nm (see Figure S3a, b in the Supporting Information). The magnified image in Figure S3b in the Supporting Information shows that there is no particle on the tip of the NW.

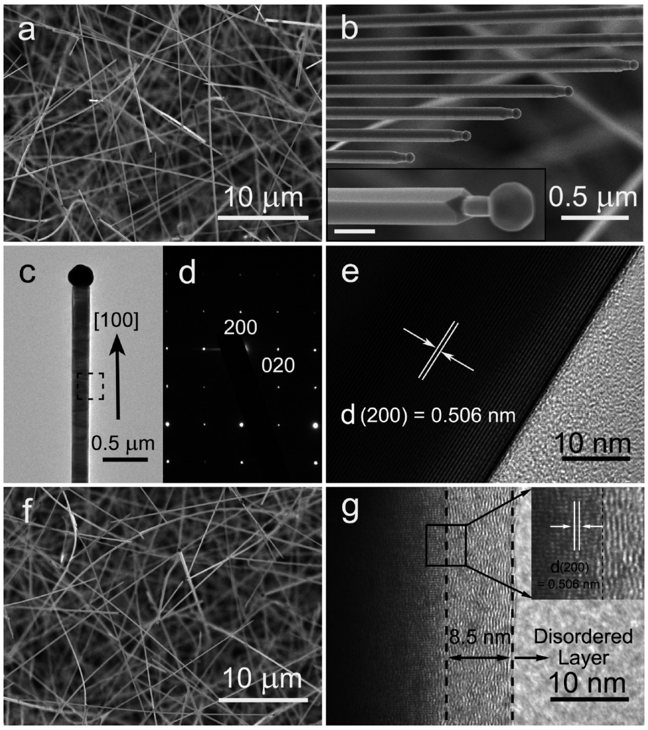

Figure 1. (a, b) Low- and high-magnification FE-SEM images of the square In_2O_3 NWs before the hydrogen treatment. The inset in b represents an enlarged single square In_2O_3 NW; Scale bar: 100 nm. (c) Low-magnification TEM image of a single In_2O_3 NW; (d, e) SAED pattern and HRTEM image of the area highlighted by the black dashed box in c before the hydrogen treatment; (f, g) Low-magnification FE-SEM and HR-TEM images of the square In_2O_3 NWs after the hydrogen treatment at 500 °C. The inset in g shows the magnified area highlighted by the black box.

The square In_2O_3 NWs are present in large abundance as shown in Figure 1a and the magnified FE-SEM image in Figure 1b clearly shows that the typical NWs have uniform widths of 100−200 nm and lengths up to hundreds of micrometers (see Figure S4 in the Supporting Information). According to the representative FE-SEM image of an individual square NW in Figure 1b, the NW has four oblique edges between adjoining smooth crystal facets and the short NW is connected to a spherical NP on top, suggesting that growth of the square NWs does not proceed by the vapor−liquid−solid (VLS) process.[30] To determine the growth direction and exposed crystal facet of the square NWs, we show in Figure 1c the FE-TEM image of an individual In_2O_3 NW. The surface is smooth and the diameter is about 200 nm. The tetragonal symmetry of the selected-area electron diffraction (SAED) pattern in Figure 1d indicates that the square NWs terminate in the {001} crystal facets. The lattice spacing of 0.506 nm belongs to the *d*-spacing of the (200) plane of the bcc structure of In_2O_3 (Figure 1e), implying that the NWs grow along the [100] direction.

The growth mechanism involves four stages as illustrated in Figure 2. In stage i, In−Au eutectic liquid droplets form. In the beginning, Au clusters form by aggregation of Au atoms on the silicon substrate, subsequently serving as the preferentially absorbed sites for In particles transferred by the carrier gas (Figure 2a). In stage ii, cylindrical NWs form by the VLS growth mechanism (Figure 2b) and in stage iii, longitudinal and radial growth of In_2O_3 NWs occurs via the combined VLS and vapor-solid (VS) growth mechanisms. It is well-known that the VLS method is a bottom-up approach. As deposition continues, In species in galore vaporize to form In oxide and they are

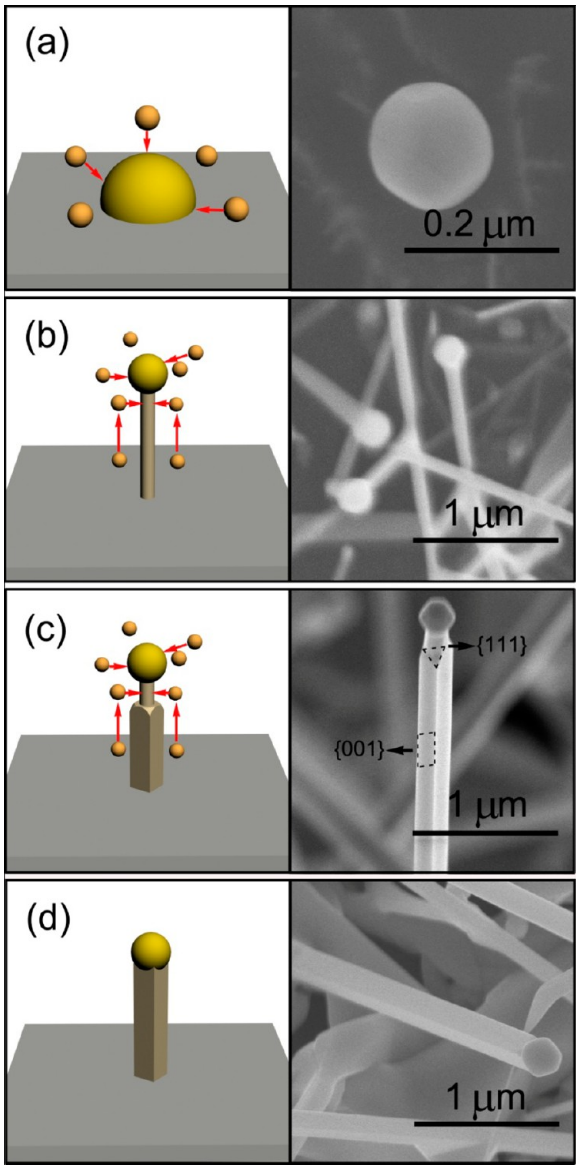

Figure 2. Schematic illustration of the growth mechanism of the square In_2O_3 NW and corresponding SEM morphology images: (a) stage i: formation of In−Au eutectic liquid droplet; (b) stage ii: formation of the cylindrical In_2O_3 NWs by the vapor−liquid−solid (VLS) mechanism during initial growth; (c) stage iii: longitudinal and radial growth of the In_2O_3 NW by the combined VLS and VS growth mechanisms; (d) stage iv: formation of square NWs with clear oblique edges and smooth {001} crystal facets.

transferred to the surface of the cylindrical NWs. For In_2O_3 with the bcc crystal structure, the surface energy follows the general sequence of (111) < (001) < (110).[31] For the cylindrical NW, the surface must include a high-index crystal facet which results in large surface energy. Low-index facets tend to form on the NW to reduce the surface energy, as evidenced by the formation of {001} and {111} crystal facets (marked by dashed rectangles and triangles). As growth continues, a large supersaturation ratio of the In_2O_3 vapor converts the oxidized In clusters to a high energy surface resulting in the appearance of the {111} facet as shown in Figure S5 in the Supporting Information. On the bottom of the NW, four {001} crystal facets form (Figure 2c).[32] In stage iv, the four oblique {111} facets vanish and square NWs with four smooth {001} crystal facets form as shown in Figure 2d.

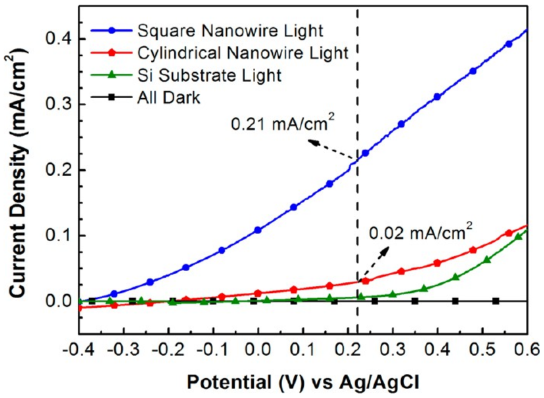

Figure 3. Current versus voltage (*J*−*V*) curves of the In_2O_3 NW photoanodes in 1 M NaOH (pH = 13.6) with Ag/AgCl being the reference electrode and Pt mesh the counter electrode. The solid circle, pentagram, and triangular curves are collected from the square, cylindrical In_2O_3 NW photoanodes and Si substrate, respectively. A dark current density curve is shown in square and the thermodynamic potential for oxygen evolution is marked by the dashed vertical line.

The effects of facet cutting on the PEC water splitting performance is investigated by comparing the linear sweep voltanmmograms acquired from the square and cylindrical In_2O_3 NWs in a deaerated (purged with N_2) three-electrode cell (see Figure S1 in the Supporting Information) containing a Pt mesh counter electrode and a Ag/AgCl reference electrode (1 mol L^{-1} NaOH-filled) with 1.0 M NaOH (pH 13.6) being the electrolyte. Figure 3 displays the current−voltage (*J*−*V*) curves obtained in darkness and under illumination by a 500 W Xe-lamp. The solid circle, pentagram and triangle curves are collected from the square, cylindrical In_2O_3 NW photoanodes, and blank Si substrate (control), respectively. The square curve represents the dark current density of both samples and it is negligible until the application of 0.6 V versus Ag/AgCl. The photocurrent density of the square In_2O_3 NWs increases from −0.4 V versus Ag/AgCl reaching 0.21 mA/cm^2 at 0.22 V versus Ag/AgCl, which is the thermodynamic potential of oxygen derived from Nernst equation: E_o (O_2/H_2O) = 1.23 − 0.05917, pH 0.42, V_{NHE} = 0.22 $V_{AgCl/Ag}$ as labeled by the dashed vertical line in Figure 3, whereas that of the cylindrical In_2O_3 NWs only reaches 0.02 mA/cm^2 at the same bias as shown by the arrow in Figure 3. In comparison, the photocurrent observed from the Si substrate is about 0.005 mA/cm^2, thus suggesting negligible contributions from the substrate to the photocurrent. To eliminate the sharp increase in the photocurrent density arising from the difference in the resistivity, the resistivity of the square and cylindrical NWs is measured by the four-point probe method. The values are 60 and 50 Ω cm, respectively, indicating that the influence of resistivity is negligible and the square NWs bound by the {001} crystal facets have superior PEC performance. This phenomenon can be explained by that the photogenerated holes from the VB are concentrated on the four {001} side facets of the square In_2O_3 NWs.[23] Specifically, owing to the {001} facets at the photoanode−electrolyte interface, the photogenerated holes in the square In_2O_3 NWs migrate to the surface and oxidize water to emit O_2. In contrast, on the cylindrical In_2O_3 NWs, the photogenerated electron−hole pairs may recombine at the isotropic NW edge surface.

Hence, {001} facet cutting is a simple and effective method to enhance the PEC performance of In_2O_3 NWs.

Although the performance of In_2O_3 NWs pertaining to water splitting can be enhanced by facet cutting, the drawback is that only a small portion of the solar spectrum is utilized in the process.[33,34] Considerable efforts have been made to improve the separation of photogenerated electrons and holes by using heterostructures and enhancing the solar light harvesting capability by these heteroarchitectures as well as by means of doping.[29,35,36] A simple and effective hydrogen treatment has been reported to reduce the band gap enabling visible light absorption and improve the electrical conductivity of the metal oxide semiconductor by introduction of a disordered layer and oxygen vacancies.[37−41] For instance, Chen and co-workers demonstrated that hydrogen-treated TiO_2 NPs exhibited a reduced bandgap of <2 eV as a result of the disordered surface shell.[37] The disordered surface layer can promote spatial separation of the photogenerated electron−hole pairs in the core of black TiO_2 giving rise to high photocatalytic efficiency.[42] Considering that the structural disorder yields band tailing and localized states, which are responsible for the reduction in the electronic gap of In_2O_3,[43] introducing disorder to the surface of the square In_2O_3 NWs by hydrogenation can conceivably improve the PEC performance.

The structure of the square In_2O_3 NWs before and after hydrogenation is assessed by FE-SEM, FE-TEM, XRD, and Raman scattering. The FE-SEM picture (Figure 1f) shows that the morphology of the In_2O_3 NWs is preserved after the hydrogen treatment, showing no obvious change in the diameter. Figure 1g and the inset show the crystal core surface of the NWs coated with a continuous disordered layer with a uniform thickness of around 8.5 nm. As shown in Figure S6a in the Supporting Information, the XRD peaks obtained from the pristine and hydrogen-treated (H-treated) In_2O_3 NWs can be indexed to bcc In_2O_3 (JCPDS card No. 06−416), indicating no change in the lattice structure after hydrogenation. Our Raman scattering also confirms this point (see Figure S6b in the Supporting Information).[44]

The current densities obtained from the pristine and H-treated In_2O_3 NW photoanodes in darkness and under illumination are plotted against the potential between −0.4 and 0.6 V versus Ag/AgCl in Figure 4a. The photocurrent density acquired from the In_2O_3 NW photoanode increases gradually as the hydrogenation temperature increases from 400 to 500 °C, but decreases if the temperature is above 500 °C. This trend is clear from the photocurrent densities obtained at a potential bias of 0.22 V versus Ag/AgCl. The photocurrent density of the pristine In_2O_3 NWs is 0.2 mA/cm^2 at 0.22 V versus Ag/AgCl, which is comparable to the value obtained from the N-doped In_2O_3 thin film photoanode.[36] The In_2O_3 NWs hydrogenated at 500 °C show a maximum value of 1.2 mA/cm^2 at 0.22 V versus Ag/AgCl, which is 5 times higher than that of the pristine In_2O_3 under the same conditions and then decreases as the temperature is further increased. In addition, current−voltage (*J*−*V*) curves are acquired under different illumination conditions using various low-pass optical filters to investigate wavelength-dependent PEC properties (see Figure S7 in the Supporting Information). The In_2O_3 NW photoanodes H-treated at 500 °C are studied for demonstration. The photocurrent densities are 1.2, 0.98, 0.84, 0.17, and 0.019 mA/cm^2 at 0.22 V versus Ag/AgCl for wavelengths of 300−700, 350−700, 400−700, 450−700, and 500−700 nm, respectively. The results indicate that the enhanced photocurrent is partly due to the increased visible absorption as a result of band gap shrinkage, and the hydrogen treatment can indeed promote the PEC performance.

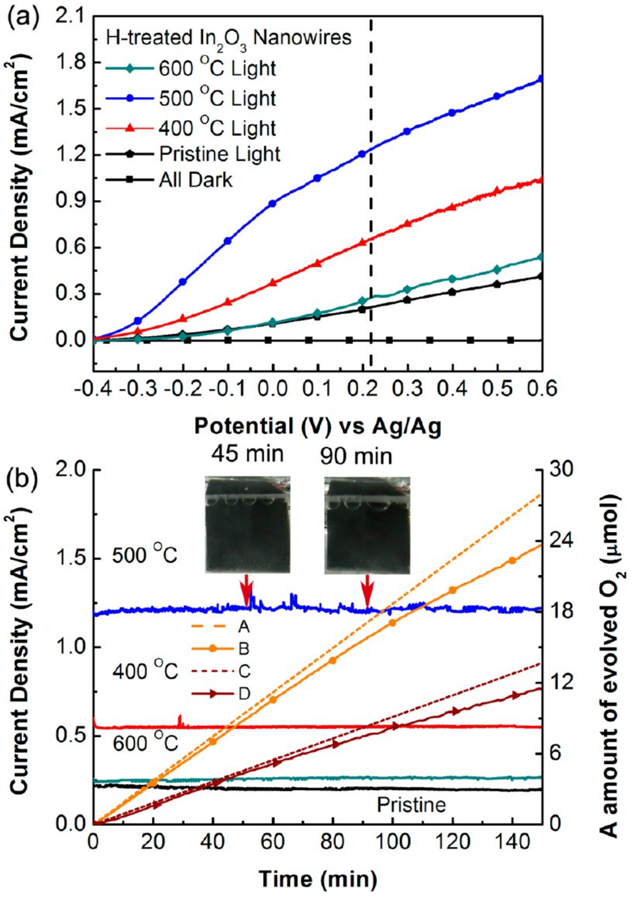

Figure 4. (a) Current versus voltage (*J*−*V*) curves of the In_2O_3 NW photoanodes H-treated at different temperatures. The curves are obtained from a 1 M aqueous NaOH (pH 13.6) solution under illumination by a 500 W Xe lamp. (b) Photocurrent versus time curves of the NW photoanodes performed at 0.22 V (versus Ag/AgCl) applied potential during the oxygen measurement. The insets are digital photos showing oxygen evolution at different time during the *I*−*t* measurement on the 500 °C H-treated In_2O_3 NW photoanode. Two groups of lines represent (A, C) the amounts of produced O_2 based on the current assuming 100% Faradic efficiency and (B, D) O_2 production measured by a fluorescent sensor; A and B are from the 500 °C H-treated In_2O_3 NWs, whereas C and D are from the 400 °C H-treated In_2O_3 NWs.

One of the practical requirements of photoanode materials is chemical stability against anodic photo-oxidation and oxygen evolution and so the stability of the pristine and H-treated In_2O_3 photoanodes and oxygen evolution is investigated. The photocurrent−time (*I*−*t*) curves are acquired at 0.22 V versus Ag/AgCl and indicated by the dashed vertical line in Figure 4b. Under illumination, stable photocurrents of 0.2, 0.6, 1.2, and 0.27 mA/cm^2 are measured from the pristine In_2O_3 NWs and In_2O_3 NWs hydrogenated at 400, 500, and 600 °C, respectively, throughout the 150 min measurement. Gas emission is observed from the In_2O_3 NW photoanodes and the insets in Figure 4b show typical digital photos taken at two different time during the I-t measurement on the 500 °C H-treated In_2O_3 NW photoanode.

To evaluate the quantity of oxygen produced from reaction, the Fraradaic efficiency is measured by a fluorescent O_2 sensor.

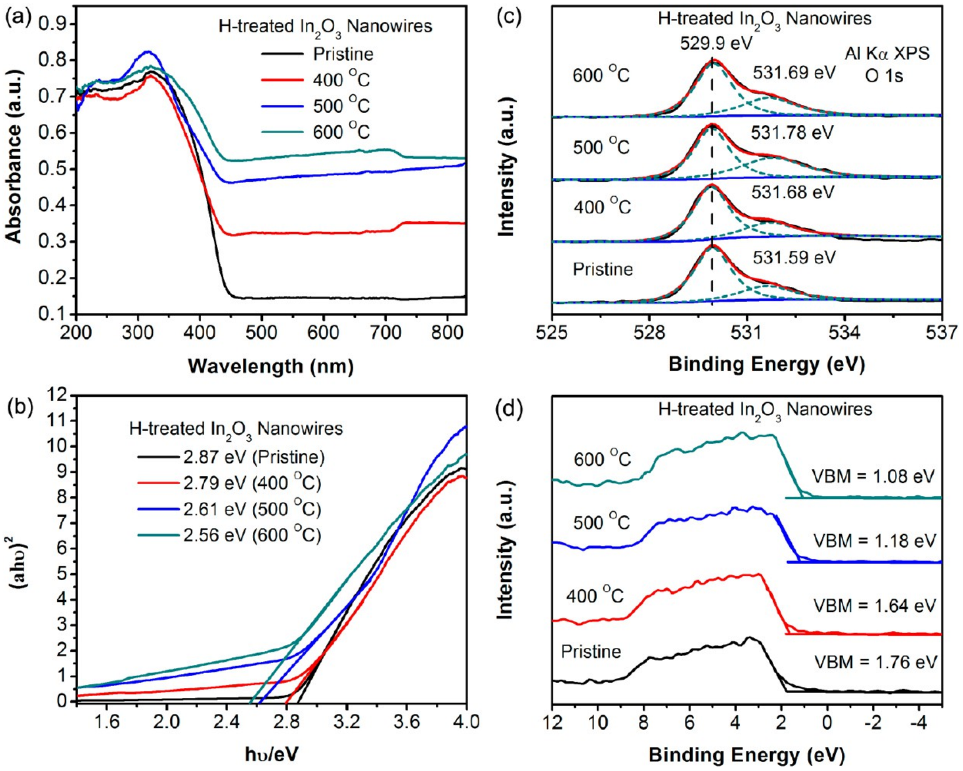

Figure 5. (a) UV−visible diffusive reflectance curves of the pristine In_2O_3 NWs (black line) and H-treated In_2O_3 NWs at 400 °C (red line), 500 (blue line), and 600 °C (green line); (b) corresponding plot of transformed Kubelka−Munk function versus the energy of light; (c) normalized O 1s XPS spectra of the pristine and H-treated In_2O_3 NWs at different temperatures. The black line represents the experimental XPS data. The red line is the fitting of the experimental data and can be decomposed into two peaks shown by the green dashed lines. (d) XPS VB spectra of the pristine (black line) and H-treated In_2O_3 NWs at temperatures of 400 (red), 500 (blue), and 600 °C (green line).

Two groups of slope lines represent the amounts of produced O_2 based on the photogenerated current assuming 100% Faradic efficiency (lines A and C in Figure 4b) and O_2 production measured by the fluorescent sensor (lines B and D, Figure 4b). Lines A and B are from the 500 °C H-treated In_2O_3 NWs and lines C and D from the 400 °C hydrogen-treated In_2O_3 NWs. The Faradaic efficiency of the In_2O_3 NW photoanodes hydrogenated at 400 and 500 °C is about 83.6 and 84.4%, respectively. No significant changes in the photocurrent, surface morphology and crystal phase are observed after continuous irradiation for 150 min, indicating that the square In_2O_3 electrode after hydrogenation is quite stable in the PEC water splitting process (see Figure S8 in the Supporting Information).

To clarify the role of hydrogen, UV−visible diffusive reflectance and XPS are conducted. Figure 5a compares the UV−vis diffusive spectra of the pristine and H-treated In_2O_3 NWs at 400, 500, and 600 °C. The large absorption at wavelengths shorter than 430 nm can be attributed to intrinsic band-to-band absorption of In_2O_3 (~2.8 eV). The pristine In_2O_3 NWs show nonzero absorption in the visible region due to small light scattering in the NW system (not caused by absorption). Compared to the pristine In_2O_3 NWs, the H-treated In_2O_3 NWs exhibit significantly increased absorption at above 430 nm as the hydrogen treatment temperature increases, indicating that the H-treated In_2O_3 NWs may utilize visible light more effectively. As shown by the plot of the Kubelka−Munk function versus the energy of the incident light absorbed by assuming that In_2O_3 is a direct semiconductor material,[44] the band gaps of the pristine and H-treated In_2O_3 NWs at 400, 500, and 600 °C are 2.87, 2.79, 2.61, and 2.56 eV, respectively (Figure 5b). The enhancement in visible-light absorption and band gap shrinkage are due to the disordered layer-induced band tail states merging with the VB and this issue will be discussed in more details later.

The change in surface bonding as a result of hydrogenation is determined by XPS. Only In, O, and C from the reference (286.4 eV) signals appear in the survey spectra acquired from the pristine and H-treated In_2O_3 NWs (Figure S9a in the Supporting Information). No apparent changes are observed from the In 3d spectra of all the samples, as shown in Figure S9b in the Supporting Information, implying that the In atoms have similar bonding after the hydrogen treatment.[12,44] On the contrary, the O 1s spectra of the pristine and H-treated In_2O_3 samples exhibit remarkable differences (see Figure S9c in the Supporting Information). The O 1s spectrum of the pristine In_2O_3 can be divided into two peaks at 529.9 and 531.6 eV as shown in Figure 5c. The peak at 529.9 eV is associated with In−O bond in In_2O_3 and that at 531.6 eV is characteristic of nonstoichiometric In oxide.[45] The In_2O_3 NWs hydrogenated at 500 °C show a broader shoulder on the high binding energy side than the pristine one. It can be deconvoluted into two peaks at 529.9 and 531.8 eV. The peak at 531.8 eV originates from the surface hydroxyl group (O−H).[33] Similar O 1s peak broadening is observed from all the samples hydrogenated at different temperature (Figure 5c). The XPS VB spectra in Figure 5d disclose that the VB edge shifts toward the vacuum level with increasing hydrogenation temperature. Linear extrapolation indicates that the VB edges are at 1.76, 1.64, 1.18, and 1.08 eV for the pristine and In_2O_3 NWs hydrogenated

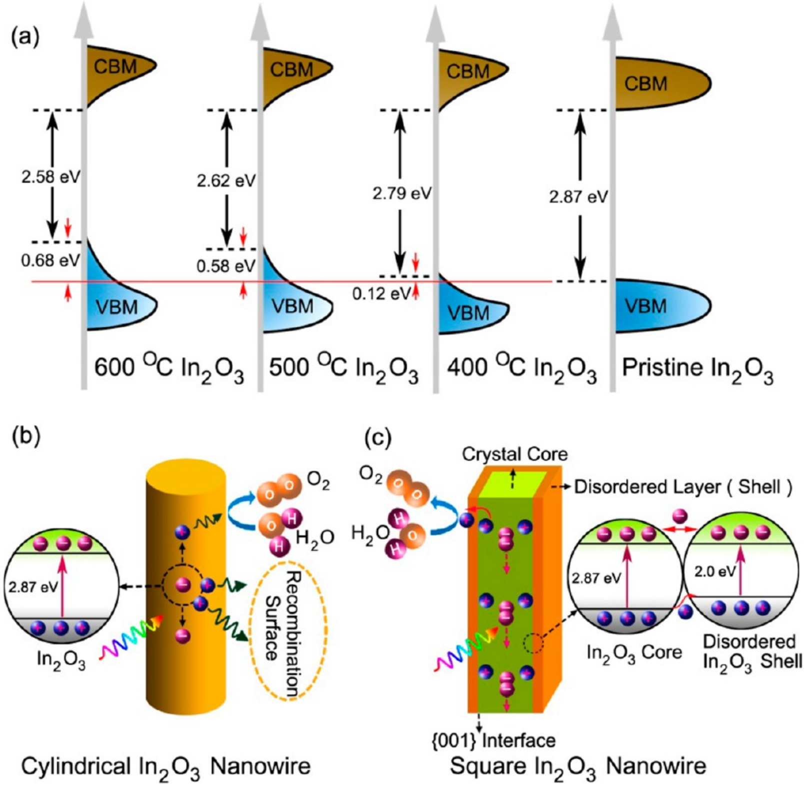

Figure 6. (a) Schematic illustration of the DOSs for the pristine and H-treated In_2O_3 NWs at different temperatures. (b, c) Schematics of PEC water splitting reaction mechanism on the cylindrical and H-treated In_2O_3 NW photoanodes, respectively.

at 400, 500, and 600 °C, respectively. By considering the bandgaps of the pristine and H-treated In_2O_3 NWs based on the absorption spectra, the CB minima are estimated to be −1.11, −1.15, −1.43, and −1.45 eV, respectively. The optical and XPS VB measurements indicate that the band gap diminishes gradually with hydrogenation temperature.

In an attempt to rationalize the enhanced optical visible absorption and band gap shrinkage after hydrogenation treatment, Chen et al. demonstrated that midgap states induced by surface disorder could upshift the VB edge of TiO_2 nanocrystals thus producing a smaller band gap,[37] whereas the H-treated and pristine TiO_2 NWs exhibited very similar VB spectra as reported previously.[39] Therefore, the enhanced visible-light absorption is due to the reduced band gap caused by the disordered layer and increased band tailor states. In this case, the In_2O_3 NWs hydrogenated at different temperatures are similar to other oxide semiconductors consisted of two phases, namely a crystal core and disordered layer shell. The densities of states (DOSs) are shown in Figure 6a. As described above, the VB edge upshifts from 1.76 to 1.18 eV as the temperature increases. Consequently, the electronic transition from VB to CB is responsible for the strong UV absorption. The enhanced visible light absorption can be ascribed to electronic transitions from the tailed VB to CB. Therefore, it is possible to use lower energy to produce electron and hole pairs to effectively improve the PEC performance of In_2O_3 NW photoanodes.

Previous investigations indicate that oxygen defects induced by hydrogenation can promote the PEC performance of metal oxide photoanode due to improvement in the electrical conductivity.[39,40,46,47] However, hydrogenation does not form the amorphous surface layer and thus oxygen vacancies may play an important role in the enhanced photocurrent. In our hydrogenated samples, modification of the photocurrent may stem from both the disordered (amorphous) surface layer and oxygen defects. However, it is difficult to determine accurately the contribution of oxygen defects only. In order to evaluate the contribution of the disordered layer to the photocurrent, the resistivity of the square In_2O_3 NWs before and after hydrogenation is measured by the four-point probe method. The results are 60, 32.5, 27.3, and 10 Ω·cm for the pristine In_2O_3 NWs and H-treated In_2O_3 NWs at 400, 500, and 600 °C, respectively. If the electrical resistance plays a key role in our materials, the photocurrent density should change with the resistance. However, the results suggest otherwise implying that the photocurrent change stems from PEC water splitting of In_2O_3.

According to our experimental results, the PEC water splitting mechanism is postulated and illustrated in Figures 6b-c. Upon irradiation with light energy larger than the band gap of In_2O_3, electrons and holes are generated in the CB and VB of the In_2O_3 NWs, respectively. The photogenerated electrons are transported to the Pt counter electrode under the external electrostatic field, followed by water reduction to produce H_2. At the same time, the photogenerated holes migrate to the In_2O_3/electrolyte interface and oxidize hydroxide ions to yield O_2. In the process, the PEC water splitting efficiency depends on the electron−hole pair separation and transportation. On the cylindrical In_2O_3, the isotropic surface resembling a spherical one renders higher charge recombination than the anisotropic side facet as shown in Figure 6b. It has been reported that the {001} facets of In_2O_3 can effectively accumulate photogenerated holes. Hence, if the square In_2O_3 NWs with the external {001} facets serve as the photoanode, the photogenerated holes will tend to transfer to the {001} facets to convert water into O_2. After hydrogenation, a distinctive interface appears between the crystal core and continuous disordered layer as shown by Figure 1g. The interface between the crystal core and disordered shell layer remains to be the {100} facet. The reported energy gap of amorphous In_2O_3 is about 2.0 eV[49] and band bending of the In_2O_3 core and shell at the interface is displayed in Figure 6c. Upon exposure to light, electrons and holes are generated in the VBs and CBs of the In_2O_3 crystal core and disordered shell by absorbing light in different wavelength regions. The holes in the In_2O_3 crystal core first accumulate on the {001} facet (Figure 6c) and are subsequently driven to the disordered shell because of the lower VBM energy of the disordered surface layer. The accumulated holes at the interface between the shell surface and electrolyte generated in both the crystal core and shell now react with hydroxide ions more readily than those in the crystalline core, as illustrated in Figure 6c. Hence, the photogenerated electron−hole pairs are effectively separated and it is responsible for the higher PEC water splitting efficiency. Shen et al. have shown that the lattice disorder can occur in a highly localized nature in the midgap state holes.[42,48] Upon irradiation, the holes may be captured by the disordered shell of the In_2O_3 NWs before arriving at the interface between the In_2O_3 and electrolyte. Therefore, an optimized disordered layer is crucial to the PEC water splitting activity and oxygen evolution. As documented in the literature,[49] the hole diffusion length is about 5−10 nm. The thickness of this disordered layer increases from 2 to 13.2 nm with hydrogenation temperature (see Figure S10 in the Supporting Information). In the thicker disordered layer on the 600 °C H-treated sample, the photogenerated holes may be trapped by the localized states before reaching the In_2O_3/electrolyte interface, thereby resulting in more substantial bulk recombination. Although the thinner disordered layer on the 400 °C H-treated NWs is beneficial to holes diffusion, the visible optical absorption is inadequate. As a result, the optimal hydrogenation temperature is 500 °C from the perspective of PEC water splitting activity.

■ CONCLUSION

Uniform square In_2O_3 NWs are produced on a large scale on crystalline silicon by chemical vapor deposition. The square In_2O_3 NWs surrounded by {001} facets deliver photocurrents which are an order of magnitude larger than those on the cylindrical In_2O_3 NWs because the photogenerated holes can accumulate on the {001} facets. The hydrogenated {001} crystal facet shows higher PEC activity due to enhanced visible optical absorption and better separation of photogenerated electrons and holes. The results demonstrate the excellent PEC water splitting performance of the hydrogenated square In_2O_3 NWs and the methodology can be extended to the design and fabrication of other NW-based core−shell structures in photoelectrical devices.

■ ASSOCIATED CONTENT

Ⓢ Supporting Information

SEM images and XRD patterns of square-shaped and cylinder-shaped In_2O_3 NWs, TEM and SAED pattern of squared-shaped In_2O_3 NW, Schematic of three-electrode electrochemical cell, XRD and Raman spectra of square-shaped In_2O_3 NWs after hydrogen treatment, SEM and XRD of In_2O_3 NWs, XPS survey spectra and In 3d of In_2O_3 NWs before and after hydrogen treatment, HRTEM images H-treated In_2O_3 NWs. This material is available free of charge via the Internet at http://pubs.acs.org.

■ AUTHOR INFORMATION

Corresponding Authors

*E-mail: hkxlwu@nju.edu.cn. Fax: 86-25-83595535. Tel: 86-83686303.

*E-mail: paul.chu@cityu.edu.hk.

Author Contributions

The manuscript was written through contributions of all authors. All authors have given approval to the final version of the manuscript.

Notes

The authors declare no competing financial interest.

■ ACKNOWLEDGMENTS

This work was supported by National Basic Research Programs of China under Grants 2011CB922102 and 2014CB339800 and National Natural Science Foundation (61264008 and 11374141). Partial support was also from PAPD and Guangdong - Hong Kong Technology Cooperation Funding Scheme (TCFS) GHP/015/12SZ.

■ REFERENCES

(1) Grätzel, M. Photoelectrochemical Cells. *Nature* **2001**, *414*, 338−344.

(2) Walter, M. G; Warren, E. L.; Mckone, J. R.; Boettcher, S. W.; Mi, Q. X.; Santori, E. A. Solar Water Splitting Cells. *Chem. Rev.* **2010**, *110*, 6446−6473.

(3) Li, Y.; Takata, T.; Cha, D.; Takanabe, K.; Minegishi, T.; Kubota, J.; Domen, K. Vertically Aligned Ta_3N_5 Nanorod Arrays for Solar-Driven Photoelectrochemical Water Splitting. *Adv. Mater.* **2013**, *25*, 125−131.

(4) Asahi, R.; Morikawa, T.; Ohwaki, T.; Aoki, K.; Taga, Y. Visible-Light Photocatalysis in Nitrogen-Doped Titanium Oxides. *Science* **2001**, *293*, 269−271.

(5) Ling, G.; Yang, H. G.; Wang, X. W.; Cheng, L.; Pan, J.; Lu, G. Q.; Cheng, H. M. Visible Light Responsive Nitrogen Doped Anatase TiO_2 Sheets with Dominant{001} Facets Derived from TiN. *J. Am. Chem. Soc.* **2009**, *131*, 12868−12869.

(6) Yang, X. Y.; Wolcott, A.; Wang, G. M.; Sobo, A.; Fitzmorris, R. C.; Qian, F.; Zhang, J. Z.; Li, Y. Nitrogen-Doped ZnO Nanowire Arrays for Photoelectrochemical Water Splitting. *Nano Lett.* **2009**, *9*, 2331−2336.

(7) Su, J. Z.; Guo, L. J.; Bao, N. Z.; Grimes, C. A. Nanostructured $WO_3/BiVO_4$ Heterojunction Films for Efficient Photoelectrochemical Water Splitting. *Nano Lett.* **2011**, *11*, 1928−1933.

(8) Mayer, M. T.; Du, C.; Wang, D. W. Hematite/Si Nanowire Dual-Absorber System for Photoelectrochemical Water Splitting at Low Applied Potentials. *J. Am. Chem. Soc.* **2012**, *134*, 12406−12409.

(9) Hou, Y.; Zuo, F.; Dagg, A.; Feng, P. Y. Visible Light-Driven α-Fe_2O_3 Nanorod/Graphene/$BiV_{1-x}Mo_xO_4$ Core/Shell Heterojunction Array for Efficient Photoelectrochemical Water Splitting. *Nano Lett.* **2012**, *12*, 6464−6473.

(10) Cho, I. S.; Chen, Z. B.; Forman, A. J.; Kim, D. R.; Rao, P. M.; Jaramillo, T. F.; Zheng, X. L. Branched TiO_2 Nanorods for Photoelectrochemical Hydrogen Production. *Nano Lett.* **2011**, *11*, 4978−4984.

(11) Su, J. Z.; Feng, X. J.; Sloppy, J. D.; Guo, L. J.; Grimes, C. A. Vertically Aligned WO_3 Nanowire Arrays Grown Directly on Transparent Conducting Oxide Coated Glass: Synthesis and Photoelectrochemical Properties. *Nano Lett.* **2011**, *11*, 203−208.

(12) Gan, J. Y.; Lu, X. H.; Zhai, T.; Zhao, Y. F.; Xie, S. L.; Mao, Y. C.; Zhang, Y. L.; Yang, Y. Y.; Tong, Y. X. Vertically Aligned In_2O_3 Nanorods on FTO Substrates for Photoelectro-chemical Applications. *J. Mater. Chem.* **2011**, *21*, 14685−14692.

(13) Barroso, M.; Cowan, A. J.; Pendlebury, S. R.; Grätzel, M.; Klug, D. R.; Durrant, J. R. The Role of Cobalt Phosphate in Enhancing the Photocatalytic Activity of α-Fe$_2$O$_3$ toward Water Oxidation. *J. Am. Chem. Soc.* **2011**, *133*, 14868−14871.

(14) Liu, M. Z.; Nam, C. Y.; Black, C. T.; Kamcev, J.; Zhang, L. H. Enhancing Water Splitting Activity and Chemical Stability of Zinc Oxide Nanowire Photoanodes with Ultrathin Titania Shells. *J. Phys. Chem. C* **2013**, *117*, 13396−13402.

(15) Mor, G. K.; Shankar, K.; Paulose, M.; Varghese, O. K.; Grimes, C. A. Enhanced Photo-cleavage of Water Using Titania Nanotube Arrays. *Nano Lett.* **2005**, *5*, 191−195.

(16) Kim, H. G.; Borse, P. H.; Jang, J. S.; Ahn, C. W.; Jeong, E. D.; Lee, J. S. Engineered Nanorod Perovskite Film Photocatalysts to Harvest Visible Light. *Adv. Mater.* **2011**, *23*, 2088−2092.

(17) Wolcott, A.; Smith, W. A.; Kuykendall, T. R.; Zhao, Y. P.; Zhang, J. Z. Photoelectro-chemical Water Splitting Using Dense and Aligned TiO$_2$ Nanorod Arrays. *Small* **2009**, *5*, 104−111.

(18) Duan, X. F.; Huang, Y.; Cui, Y.; Wang, J. F.; Lieber, C. M. Indium Phosphide Nanowires as Building Blocks for Nanoscale Electronic and Optoelectronic Devices. *Nature* **2001**, *409*, 66−69.

(19) Hu, J. T.; Ouyang, M.; Yang, P. D.; Lieber, C. M. Controlled Growth and Electrical Properties of Heterojunctions of Carbon Nanotubes and Silicon Nanowires. *Nature* **1999**, *399*, 48−51.

(20) Mor, G. K.; Shankar, K.; Paulose, M.; Varghese, O. K.; Grimes, C. A. Use of Highly-Ordered TiO$_2$ Nanotube Arrays in Dye-Sensitized Solar Cells. *Nano Lett.* **2006**, *6*, 215−218.

(21) Oh, I.; Kye, J.; Hwang, S. Enhanced Photoelectrochemical Hydrogen Production from Silicon Nanowire Array Photocathode. *Nano Lett.* **2012**, *12*, 298−302.

(22) Yang, P. D. Crystal Cuts on the Nanoscale. *Nature* **2011**, *482*, 41−42.

(23) Sun, M.; Xiong, S. J.; Wu, X. L.; He, C. Y.; Li, T. H.; Chu, P. K. Enhanced Photocatalytic Oxygen Evolution by Crystal Cutting. *Adv. Mater.* **2013**, *25*, 2035−2039.

(24) Ho, J. Y.; Huang, M. H. Synthesis of Submicrometer-Sized Cu$_2$O Crystals with Morphological Evolution from Cubic to Hexapod Structures and Their Comparative Photo-catalytic Activity. *J. Phys. Chem. C* **2009**, *113*, 14159−14164.

(25) Huang, W. C.; Lyu, L. M.; Yang, Y. C.; Huang, M. H. Synthesis of Cu$_2$O Nanocrystals from Cubic to Rhombic Dodecahedral Structures and Their Comparative Photocatalytic Activity. *J. Am. Chem. Soc.* **2011**, *134*, 1261−1267.

(26) Pan, J.; Liu, G.; Lu, G. Q.; Cheng, H. M. On the True Photoreactivity Order of {001}, {010}, and {101} Facets of Anatase TiO$_2$ Crystals. *Angew. Chem., Int. Ed.* **2011**, *50*, 2133−2137.

(27) Zheng, Z. K.; Huang, B. B.; Lu, J. B.; Qin, X. Y.; Zhang, X. Y.; Dai, Y. Hierarchical TiO$_2$ Microspheres: Synergetic Effect of {001} and {101} Facets for Enhanced Photocatalytic Activity. *Chem.—Eur. J.* **2011**, *17*, 15032−15038.

(28) Zheng, Z. K.; Huang, B. B.; Wang, Z. Y.; Guo, M.; Qin, X. Y.; Zhang, X. Y.; Wang, P.; Dai, Y. Crystal Faces of Cu$_2$O and Their Stabilities in Photocatalytic Reactions. *J. Phys. Chem. C* **2009**, *113*, 14448−14453.

(29) Mu, J. B.; Chen, B.; Zhang, M. Y.; Guo, Z. C.; Zhang, P.; Zhang, Z. Y.; Sun, Y. Y.; Shao, C. L.; Liu, Y. C. Enhancement of the Visible-Light Photocatalytic Activity of In$_2$O$_3$−TiO$_2$ Nanofiber Heteroarchitectures. *ACS Appl. Mater. Interfaces* **2012**, *4*, 424−430.

(30) Yan, Y. G.; Zhang, Y.; Zeng, H. G.; Zhang, J. X.; Cao, X. L.; Zhang, L. D. Tunable Synthesis of In$_2$O$_3$ Nanowires, Nanoarrows and Nanorods. *Nanotechnology* **2007**, *18*, 175601.

(31) Wang, Z. L. Transmission Electron Microscopy of Shape-Controlled Nanocrystals and Their Assemblies. *J. Phys. Chem. B* **2000**, *104*, 1153−1175.

(32) Yan, Y. G.; Zhou, L. X.; Zhang, Y.; Zhang, J.; Hu, S. Q. Large-Scale Synthesis of In$_2$O$_3$ Nanocubes Under Nondynamic Equilibrium Model. *Cryst. Growth Des.* **2008**, *8*, 3285−3289.

(33) Mu, J. B.; Shao, C. L.; Guo, Z. C.; Zhang, M. Y.; Zhang, Z. Y.; Zhang, P.; Chen, B.; Liu, Y. C. In$_2$O$_3$ Nanocubes/Carbon Nanofibers Heterostructures with High Visible Light Photocatalytic Activity. *J. Mater. Chem.* **2012**, *22*, 1786−1793.

(34) McCann, J. F.; Bockris, J. Photoelectrochemical Properties of n-Type In$_2$O$_3$. *J. Electrochem. Soc.* **1981**, *128*, 1719−1723.

(35) Reyes-Gil, K. R.; Sun, Y. P.; Reyes-García, E.; Raftery, D. Characterization of Photoactive Centers in N-Doped In$_2$O$_3$ Visible Photocatalysts for Water Oxidation. *J. Phys. Chem. C.* **2009**, *113*, 12558−12570.

(36) Reyes-Gil, K. R.; Reyes-García, E. A.; Raftery, D. Nitrogen-Doped In$_2$O$_3$ Thin Film Electrodes for Photocatalytic Water Splitting. *J. Phys. Chem. C* **2007**, *111*, 14579−14588.

(37) Chen, X. B.; Liu, L.; Yu, P. Y.; Mao, S. S. Increasing Solar Absorption for Photocatalysis with Black Hydrogenated Titanium Dioxide Nanocrystals. *Science* **2011**, *331*, 746−750.

(38) Naldoni, A.; Allieta, M.; Santangelo, S.; Marelli, M.; Fabbri, F.; Cappelli, S.; Bianchi, C. L.; Psaro, R.; Santo, V. D. Effect of Nature and Location of Defects on Bandgap Narrowing in Black TiO$_2$ Nanoparticles. *J. Am. Chem. Soc.* **2012**, *134*, 7600−7603.

(39) Wang, G. M.; Wang, H. Y.; Ling, Y. C.; Tang, Y. C.; Yang, X. Y.; Fitzmorris, R. C.; Wang, C. C.; Zhang, J. Z.; Li, Y. Hydrogen-Treated TiO$_2$ Nanowire Arrays for Photoelectrochemical Water Splitting. *Nano Lett.* **2011**, *11*, 3026−3033.

(40) Wang, G. M.; Ling, Y. C.; Wang, H. Y.; Yang, X. Y.; Wang, C. C.; Zhang, J. Z.; Li, Y. Hydrogen-treated WO$_3$ Nanoflakes Show Enhanced Photostability. *Energy Environ. Sci.* **2012**, *5*, 6180−6187.

(41) Yao, C. Z.; Wei, B. H.; Ma, H. X.; Li, H.; Meng, L. X.; Zhang, X. S.; Gong, Q. J. Enhanced Photoelectrochemical Performance of Hydrogenated ZnO Hierarchical Nanorod Arrays. *J. Power Sources* **2013**, *237*, 295−299.

(42) Liu, L.; Yu, P. Y.; Chen, X. B.; Mao, S. S.; Shen, D. Z. Hydrogenation and Disorder in Engineered Black TiO$_2$. *Phys. Rev. Lett.* **2013**, *111*, 065505.

(43) Aliano, A.; Catellani, A.; Cicero, G. Characterization of Amorphous In$_2$O$_3$: An ab initio Molecular Dynamics Study. *Appl. Phys. Lett.* **2011**, *99*, 211903.

(44) Gan, J. Y.; Lu, X. H.; Wu, J. H.; Xie, S. L.; Zhai, T.; Yu, M. H.; Zhang, Z. H.; Mao, Y. C.; Wang, S. C.; Shen, Y.; Tong, Y. X. Oxygen Vacancies Promoting Photoelectrochemical Performance of In$_2$O$_3$ Nanocubes. *Sci. Rep.* **2013**, *3*, 1021.

(45) Gai, L. G.; Ma, L.; Jiang, H. H.; Ma, Y.; Tian, Y.; Liu, H. Nitrogen-doped In$_2$O$_3$ Nanocrystals Constituting Hierarchical Structures with Enhanced Gas-sensing Properties. *CrystEngComm* **2012**, *14*, 7479−7486.

(46) Wang, G. M.; Ling, Y. C.; Li, Y. Oxygen-Deficient Metal Oxide Nanostructures for Photoelectrochemical Water oxidation and Other Applications. *Nanoscale* **2012**, *4*, 6682−6691.

(47) Lu, X. H.; Wang, G. M.; Xie, S. L.; Shi, J. Y.; Li, W.; Tong, Y. X.; Li, Y. Efficient Photocatalytic Hydrogen Evolution over Hydrogenated ZnO Nanorod Arrays. *Chem. Commun.* **2012**, *48*, 7717−7719.

(48) Ulutas, K.; Deger, D.; Skarlatos, Y. Thickness Dependence of Optical Properties of Amorphous Indium Oxide Thin Films Deposited by Reactive Evaporation. *Phys. Status Solidi A* **2006**, *203*, 2432−2437.

(49) Wang, L.; Lee, C. Y.; Schmuki, P. Solar Water Splitting: Preserving the Beneficial Small Feature Size in Porous α-Fe$_2$O$_3$ Photoelectrodes During Annealing. *J. Mater. Chem. A* **2013**, *1*, 212−215.